Journal of Sound and Vibration 327 (2009) 211–230

Contents lists available at ScienceDirect

Journal of Sound and Vibration

journal homepage: www.elsevier.com/locate/jsvi

Nonlinear vibrations and imperfection sensitivity of a cylindrical shell containing axial fluid flow

Z. del Prado [a], P.B. Gonçalves [b,*], M.P. Païdoussis [c]

[a] Department of Civil Engineering, Federal University of Goiás, 74605-200 Goiânia, GO, Brazil
[b] Department of Civil Engineering, Catholic University, PUC-Rio, 22453-900 Rio de Janeiro, RJ, Brazil
[c] Department of Mechanical Engineering, McGill University, 817 Sherbrooke Street W., Montreal, Québec, Canada H3A 2K6

ARTICLE INFO

Article history:
Received 5 May 2008
Received in revised form
23 May 2009
Accepted 16 June 2009
Handling Editor: C.L. Morfey
Available online 10 July 2009

ABSTRACT

The high imperfection sensitivity of cylindrical shells under static compressive axial loads is a well-known phenomenon in structural stability. On the other hand, less is known of the influence of imperfections on the nonlinear vibrations of these shells under harmonic axial loads. The aim of this work is to study the simultaneous influence of geometric imperfections and an axial fluid flow on the nonlinear vibrations and instabilities of simply supported circular cylindrical shells under axial load. The fluid is assumed to be non-viscous and incompressible and the flow to be isentropic and irrotational. The behavior of the thin-walled shell is modeled by Donnell's nonlinear shallow-shell equations. It is subjected to a static uniform compressive axial pre-load plus a harmonic axial load. A low-dimensional modal expansion, which satisfies the relevant boundary and continuity conditions, and takes into account all relevant nonlinear modal interactions observed in the past in the nonlinear vibrations of cylindrical shells with and without flow is used together with the Galerkin method to derive a set of eight coupled nonlinear ordinary differential equations of motion which are, in turn, solved by the Runge–Kutta method. The shell is considered to be initially at rest, in a position corresponding to a pre-buckling configuration. Then, a harmonic excitation is applied and conditions for parametric instability and dynamic snap-through are sought. The results clarify the marked influence of geometric imperfections and fluid flow on the dynamic stability boundaries, bifurcations and basins of attraction.

1. Introduction

The combination of a simple geometry and proficiency as a load carrying member, particularly for axial loads and lateral pressure, makes cylindrical shells one of the most common shell geometries in industrial applications and in nature. Examples can be found in different engineering branches such as civil, mechanical, nuclear, aerospace and off-shore engineering. In most of these applications cylindrical shells are used to hold or transport fluids. So, for decades, the study of shell–fluid interaction considering a quiescent or flowing fluid has been an important research area in applied mechanics.

It is a well-established fact, backed by a large collection of theoretical and experimental results, that cylindrical shells under several types of static load, such as axial compression, external pressure, torsion and bending, are liable to buckling and may display a load capacity much lower than the theoretical critical load, due mainly to the effect of imperfections [1]. The most deleterious imperfections in thin cylindrical shells are the initial geometric imperfections. This is mainly due to the highly nonlinear behavior of cylindrical shells and the reduction of membrane stiffness, modal coupling and

---

[*] Corresponding author. Tel.: +55 21 3527 1188; fax: +55 21 3527 9158.
E-mail address: paulo@puc-rio.br (P.B. Gonçalves).

0022-460X/$ - see front matter © 2009 Elsevier Ltd. All rights reserved.
doi:10.1016/j.jsv.2009.06.016

interactions generated by the imperfections. Experimental results on thin cylindrical shells under static axial compression show that they may lose stability at load levels as low as a fraction of the material's ultimate strength [1]. In order to take into account the effect of usually unknown imperfections in design, theoretical lower-bounds, based on nonlinear analysis of the imperfect structure, have been proposed in the literature [2]. However, the influence of these geometric imperfections on the vibration characteristics and nonlinear oscillations of thin shells is not well understood. In a dynamic environment, several parameters may influence the imperfection sensitivity, such as initial conditions and load characteristics. The addition of fluid forces makes this problem even more complicated [3]. Also, changes in the effective stiffness due to the static pre-loading may affect drastically the dynamic response and stability characteristics of these systems [4]. Finally, controlled experiments on cylindrical shells under dynamic loads are much more difficult to perform and rare than in the static case [5–7].

Due to these facts, the study of the dynamics of cylindrical shells is one of the most challenging problems in nonlinear dynamics. Although geometrical imperfections play an important role in the shell response [8,9], the great majority of the investigations are concerned with the study of perfect structures. Also, most of these studies deal with the analysis of shells vibrating in vacuum. Fewer studies are focused on the analysis of the nonlinear vibrations of cylindrical shells in contact with a dense fluid.

In Amabili and Païdoussis [10] and Karagiosis [11], one can find very extensive literature reviews related to the nonlinear dynamics of shells in vacuum, and shells filled with or surrounded by quiescent or flowing fluids. These topics are also present in detail in the books by Païdoussis on fluid–structure interactions [3] and Amabili on nonlinear vibrations and stability of shells and plates [12]. Here only a few key contributions will be mentioned.

The seminal work of Evensen [13] and Dowell and Ventres [14] gave the original idea to the modal expansions of the shell flexural displacement involving the symmetric and asymmetric modes; later, the studies of Ginsberg [15] and Chen and Babcock [16] contributed to the understanding of the influence of the companion mode on the behavior of cylindrical shells. In the fundamental work of Gonçalves and Batista [17] it was found that the presence of a dense fluid in the shell, increases the softening characteristics of the frequency–amplitude relation when compared with the results for the same shell in vacuum. In a series of important papers, Amabili et al. [18–21] studied the nonlinear free and forced vibrations of a simply supported, circular cylindrical shell in contact with an incompressible and inviscid, quiescent or flowing dense fluid, using Donnell's nonlinear shallow-shell theory.

The effect of initial geometric imperfections on the dynamics of cylindrical shells has been less studied than in the static case. Watawala and Nash [22] studied the influence of initial geometric imperfections on the free vibrations of fluid-filled cylindrical shells and subject to seismic motions of the base. Amabili and Pellicano [23] studied the nonlinear stability of simply supported, circular cylindrical shells in supersonic axial flow using Donnell's nonlinear shallow-shell theory, considering asymmetric and axisymmetric geometric imperfections. Amabili [24], using an accurate modal expansion, studied the large-amplitude response of perfect and imperfect, simply supported circular cylindrical shells subjected to harmonic excitation in the neighborhood of some of the lowest natural frequencies. Pellicano and Amabili [25], using both Donnell's nonlinear shallow-shell and Sanders–Koiter shell theories, analyzed the dynamic stability of cylindrical shells in the presence of static and dynamic axial loads, geometric imperfections and fluid–structure interaction. Catellani et al. [7] analyzed the static and dynamic behavior of a compressed circular cylindrical shell with geometric imperfections using Donnell's nonlinear shallow-shell theory.

In this paper, an eight-degree-of-freedom model is used to study the nonlinear oscillations and instabilities of perfect and imperfect axially loaded circular cylindrical shells with internal flowing fluid. The shell is subjected to axial time-dependent loading, composed of two terms: a constant term and a harmonic one. To discretize the shell, the Donnell shallow-shell equations are used together with the Galerkin method to derive a set of coupled ordinary differential equations of motion. In order to study the nonlinear behavior of the shell, several numerical strategies were used to obtain Poincaré maps, stability boundaries, basins of attraction and bifurcation diagrams [26].

The main interest of this investigation is to study the simultaneous effects of initial geometric imperfections and an internal flowing fluid on the nonlinear behavior of the pre-stressed thin-walled cylindrical shell. In particular, the influence of imperfections and fluid velocity on the stability boundaries in control space, bifurcation diagrams, critical loads and the geometry and topology of basins of attraction are studied in detail in the vicinity of the most important resonance regions of the axially excited shell. The combination of axial load, imperfections and fluid flow leads to a complex dynamical behavior, which can only be clarified through a detailed parametric analysis. In this scenario, the importance of accurate low-dimensional models for shell nonlinear analysis becomes evident [27–30]. To the authors' knowledge, such an investigation combining all the aforementioned perturbation sources has not been presented so far.

2. Mathematical formulation

2.1. Shell equations

Consider an imperfect thin-walled circular cylindrical shell of radius R, length L, and thickness h, containing flowing fluid. The shell is assumed to be made of an elastic, homogeneous and isotropic material with Young's modulus E, Poisson ratio ν, and mass density ρ_S. The axial, circumferential and radial coordinates are denoted by x, y and z, respectively, and the corresponding displacements on the shell surface are denoted by u, v and w, as shown in Fig. 1. In this work the mathematical formulation will follow that previously presented in Refs. [4,9,18,25].

The shell is subjected to an internal flowing fluid and a uniformly distributed axial load along the edges $x = 0$ and L, given by

$$\tilde{N}_x(t) = -\frac{P_e}{2\pi R} - \frac{P_d}{2\pi R}\cos(\omega t), \tag{1}$$

where P_e is a compressive uniform static load, P_d is the magnitude of the harmonic axial load, t is the time and ω is the forcing angular frequency.

The nonlinear equation of motion, based on the von Kármán–Donnell shallow-shell theory, in terms of a stress function F, the radial displacement w and an initial geometric imperfection field w_0, is given by

$$\begin{aligned} D\nabla^4 w + ch\dot{w} + \rho_s h\ddot{w} = f - P_h + \frac{1}{R}\frac{\partial^2 F}{\partial x^2} + \frac{1}{R}\left[\frac{\partial^2 F}{\partial \theta^2}\left(\frac{\partial^2 w}{\partial x^2} + \frac{\partial^2 w_0}{\partial x^2}\right) - 2\frac{\partial^2 F}{\partial x\partial\theta}\left(\frac{\partial^2 w}{\partial x\partial\theta} + \frac{\partial^2 w_0}{\partial x\partial\theta}\right)\right. \\ \left. + \frac{\partial^2 F}{\partial x^2}\left(\frac{\partial^2 w}{\partial \theta^2} + \frac{\partial^2 w_0}{\partial \theta^2}\right)\right], \end{aligned} \tag{2}$$

where $D = Eh^3/[12(1-\nu^2)]$ is the flexural rigidity, c (kg/m^3 s) is the damping coefficient, and f and P_h are the radial pressures applied to the surface of the shell as a consequence of, respectively, external forces and the contained flowing fluid.

The compatibility equation is given by

$$\frac{1}{Eh}\nabla^4 F = -\frac{1}{R}\frac{\partial^2 w}{\partial x^2} - \frac{1}{R^2}\left[-\left(\frac{\partial w}{\partial x\partial\theta}\right)^2 - 2\frac{\partial^2 w}{\partial x\partial\theta}\frac{\partial^2 w_0}{\partial x\partial\theta} + \left(\frac{\partial^2 w}{\partial x^2} + \frac{\partial^2 w_0}{\partial x^2}\right)\frac{\partial^2 w}{\partial\theta^2} + \frac{\partial^2 w}{\partial x^2}\frac{\partial^2 w_0}{\partial\theta^2}\right]. \tag{3}$$

In Eqs. (2) and (3) the bi-harmonic operator is defined as $\nabla^4 = [\partial^2/\partial x^2 + \partial^2/(R^2\partial\theta^2)]^2$.

2.2. In-plane stresses and boundary conditions

The forces per unit length in the axial and circumferential directions, as well as the shear force are given in terms of the stress function by [31]

$$N_x = \frac{1}{R^2}\frac{\partial^2 F}{\partial\theta^2}, \quad N_\theta = \frac{\partial^2 F}{\partial x^2}, \quad N_{x\theta} = -\frac{1}{R}\frac{\partial^2 F}{\partial x\partial\theta}. \tag{4}$$

The force–displacement relationships are

$$(1-\nu^2)\frac{N_x}{Eh} = -\nu\frac{w}{R} + \frac{1}{2}\left(\frac{\partial w}{\partial x}\right)^2 + \frac{\partial w}{\partial x}\frac{\partial w_0}{\partial x} + \nu\frac{1}{2}\left(\frac{1}{R}\frac{\partial w}{\partial\theta}\right)^2 + \nu\frac{1}{R}\frac{\partial w}{\partial\theta}\frac{1}{R}\frac{\partial w_0}{\partial\theta} + \frac{\partial u}{\partial\theta} + \nu\frac{1}{R}\frac{\partial v}{\partial\theta}, \tag{5}$$

$$(1-\nu^2)\frac{N_\theta}{Eh} = -\frac{w}{R} + \frac{\nu}{2}\left(\frac{\partial w}{\partial x}\right)^2 + \nu\frac{\partial w}{\partial x}\frac{\partial w_0}{\partial x} + \frac{1}{2}\left(\frac{1}{R}\frac{\partial w}{\partial\theta}\right)^2 + \frac{1}{R}\frac{\partial w}{\partial\theta}\frac{1}{R}\frac{\partial w_0}{\partial\theta} + \nu\frac{\partial u}{\partial x} + \frac{1}{R}\frac{\partial v}{\partial\theta}, \tag{6}$$

$$(1-\nu^2)\frac{N_{x\theta}}{Eh} = 2(1-\nu)\left[\frac{1}{R}\frac{\partial w}{\partial x}\frac{\partial w}{\partial\theta} + \frac{1}{R}\frac{\partial w}{\partial x}\frac{\partial w_0}{\partial x} + \frac{1}{R}\frac{\partial w_0}{\partial x}\frac{\partial w}{\partial\theta} + \frac{1}{R}\frac{\partial u}{\partial\theta} + \frac{\partial v}{\partial x}\right]. \tag{7}$$

The simply supported boundary conditions for the shell are

$$w = w_0 = 0 \quad \text{for } x = 0, L, \tag{8}$$

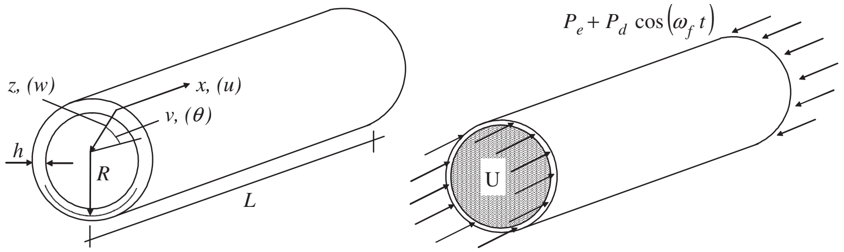

Fig. 1. Shell geometry.

and

$$M_x = -D\left[\frac{\partial^2 w}{\partial x^2} + \nu\left(\frac{1}{R^2}\frac{\partial^2 w}{\partial \theta^2}\right)\right] = 0 \quad \text{for } x = 0, L, \tag{9}$$

$$\frac{\partial^2 w_0}{\partial x^2} = 0, \quad \overline{N}_x = \tilde{N}_x(t) \quad \text{and} \quad v = 0 \ \text{ for } x = 0, L. \tag{10}$$

2.3. Solution expansion for the transverse displacement

The numerical model is developed by expanding the radial displacement w in series form in the circumferential and axial variables. From previous investigations on modal solutions for the nonlinear analysis of cylindrical shells under axial fluid flow, a suitable expansion for the present problem is as follows [3,18]:

$$\begin{aligned} w(x,\theta,t) = {} & \xi_{1,1}(t)h\sin(qx)\cos(n\theta) + \xi_{1,1c}(t)h\sin(qx)\sin(n\theta) \\ & + \xi_{2,1}(t)h\sin(2qx)\cos(n\theta) + \xi_{2,1c}(t)h\sin(2qx)\sin(n\theta) \\ & + \xi_{0,1}(t)h\sin(qx) + \xi_{0,3}(t)h\sin(3qx) + \xi_{0,5}(t)h\sin(5qx) \\ & + \xi_{0,7}(t)h\sin(7qx), \end{aligned} \tag{11}$$

where $\xi_{1,1}(t)$, $\xi_{1,1c}(t)$, $\xi_{2,1}(t)$, $\xi_{2,1c}(t)$, $\xi_{0,1}(t)$, $\xi_{0,3}(t)$, $\xi_{0,5}(t)$ and $\xi_{0,7}(t)$ are the time-dependent modal amplitudes, $q = m\pi/L$ and m and n are, respectively, the number of half-waves in the axial direction and the number of waves in the radial direction. This leads to an eight-degree-of-freedom reduced order model. This model includes the basic vibration (driven) mode, its companion mode, four axisymmetric modes and the gyroscopic modes (driven and companion) with twice the number of waves in the axial direction as the basic vibration mode, which becomes important at high flow velocities [3,12]. These modes are essential to describe the most important nonlinear interactions observed in cylindrical shells under axial fluid flow and sufficient for our purposes. However, more refined modal solutions can be found in the literature [12].

Based on the fact that the most deleterious imperfections are those that lead to the strongest coupling with the modes adopted in (11) through the quadratic and cubic nonlinearities in Eqs. (2) and (3), the geometric imperfections are described here as a linear combination of the same modes included in the lateral displacement expansion, namely

$$\begin{aligned} w_0(x,\theta) = {} & \Xi_{1,1}h\sin(qx)\cos(n\theta) + \Xi_{1,1c}h\sin(qx)\sin(n\theta) + \Xi_{2,1}(t)h\sin(2qx)\cos(n\theta) \\ & + \Xi_{2,1c}(t)h\sin(2qx)\sin(n\theta) + \Xi_{0,1}h\sin(qx) + \Xi_{0,3}h\sin(3qx) + \Xi_{0,4}h\sin(5qx) + \Xi_{0,5}h\sin(7qx), \end{aligned} \tag{12}$$

where $\Xi_{1,1}$, $\Xi_{1,1c}$, $\Xi_{2,1}$, $\Xi_{2,1c}$, $\Xi_{0,1}$, $\Xi_{0,3}$, $\Xi_{0,5}$, $\Xi_{0,7}$ are the imperfection amplitudes.

The solution for the stress function may be written as $F = F_h + F_p$, where F_h is the homogeneous solution and F_p the particular solution. The particular solution F_p is obtained analytically by substituting the assumed form of the lateral deflection, w, Eq. (11), and the geometric imperfection, w_0, Eq. (12), on the right-hand side of the compatibility equation (3), and by solving the resulting linear partial differential equation together with the relevant boundary and continuity conditions.

The homogeneous part of the stress function can be written as

$$F_h = \frac{1}{2}\overline{N}_x R^2\theta^2 + \frac{1}{2}x^2\left\{\overline{N}_\theta - \frac{1}{2\pi RL}\int_0^{2\pi}\int_0^L \frac{\partial^2 F_p}{\partial x^2} R\,\mathrm{d}\theta\,\mathrm{d}x\right\} - \overline{N}_{x\theta}R\theta, \tag{13}$$

where $\overline{N}_x$, $\overline{N}_\theta$ and $\overline{N}_{x\theta}$ are the average in-plane restraint stresses generated at the ends of the shell. This solution enables one to satisfy the in-plane boundary conditions on the average [9,18].

The expansion for the radial displacement w and for the imperfection w_0 satisfy the out-of-plane boundary conditions (8) and (9) and the continuity of the circumferential displacement v:

$$\int_0^{2\pi}\frac{\partial v}{\partial \theta}\,\mathrm{d}\theta = \int_0^{2\pi}\left[\frac{1}{Eh}\left(\frac{\partial^2 F}{\partial x^2} - \nu\frac{1}{R^2}\frac{\partial^2 F}{\partial \theta^2}\right) + \frac{w}{R} - \frac{1}{2}\left(\frac{1}{R}\frac{\partial F}{\partial \theta}\right)^2\right]\mathrm{d}\theta = 0, \tag{14}$$

and the homogeneous part of the stress function satisfies the in-plane boundary conditions, Eq. (10), on the average, i.e.,

$$\int_0^{2\pi} N_x R\,\mathrm{d}\theta = 2\pi R\tilde{N}_x(t), \quad \int_0^{2\pi}\int_0^L N_{x\theta}R\,\mathrm{d}x\,\mathrm{d}\theta = 0. \tag{15}$$

Boundary conditions (15) allow us to express the in-plane restraint stresses N_x, N_θ and $N_{x\theta}$ in terms of w and its derivatives [8,9]:

$$\overline{N}_x = \tilde{N}_x, \tag{16}$$

$$\overline{N}_\theta = \nu \tilde{N}_x + \frac{Eh}{2\pi L}\int_0^{2\pi}\int_0^L \left[-\frac{w}{R}+\frac{1}{2}\left(\frac{1}{R}\frac{\partial w}{\partial \theta}\right)^2\right]\mathrm{d}x\,\mathrm{d}\theta, \tag{17}$$

$$\overline{N}_{x\theta} = 0. \tag{18}$$

Upon substituting the modal expressions for F, w and w_0 into Eq. (2) and applying the Galerkin method, a set of six nonlinear ordinary differential equations is obtained in terms of the time-dependent modal amplitudes $\xi(t)_{i,j}$, having as coefficients the imperfection amplitudes $\Xi_{i,j}$.

2.4. Modeling of fluid–structure interaction

To determine the perturbation pressure on the shell wall, the Païdoussis and Denise [3] model will be adopted. In this model, linear potential theory is used to describe the effect of the internal axially flowing fluid. The fluid is assumed to be incompressible and non-viscous and the flow to be isentropic and irrotational. The irrotationality property is the condition for the existence of a scalar potential function Ψ, from which the velocity may be written as

$$V = -\nabla \Psi. \tag{19}$$

This potential function is equal to$\Psi = -Ux + \Phi$, where the first term is associated with the undisturbed mean flow velocity U, and the second term, the unsteady component Φ is associated with the shell motion. The function Φ must satisfy the Laplace equation and the impenetrability condition at the shell–fluid interface.

The potential function satisfies the continuity equation. Following the procedure presented in previous studies [3], the perturbation pressure on the shell wall is found to be

$$P_h = \rho_F \frac{L}{m\pi}\frac{\mathrm{I}_n(m\pi R/L)}{\mathrm{I}'_n(m\pi R/L)}\left(\frac{\partial^2 w}{\partial t^2} + 2U\frac{\partial^2 w}{\partial t \partial x} + U^2\frac{\partial^2 w}{\partial x^2}\right), \tag{20}$$

where ρ_F is the fluid density; I_n is the nth order modified Bessel function of the first kind and I'_n is the derivative with respect to its argument.

3. Results

Consider a thin-walled cylindrical shell with $h = 0.002$ m, $R = 0.2$ m, $L = 0.4$ m, $E = 2.1\times10^8$ kN/m^2, $\nu = 0.3$, $\rho_S = 7850$ kg/m^3 and $\rho_F = 1000$ kg/m^3 [4,8]. For this geometry, the classical buckling load is equal to $P_{\mathrm{cr}} = 2541.95$ kN/m [31] and occurs for $(n,m) = (5,1)$; and the critical flow velocity is $U_{\mathrm{cr}} = 257.53$ m/s. The lowest natural frequency of the fluid-filled shell is $\omega_0 = 1704.33$ rad/s, which also occurs for $(n,m) = (5,1)$. The damping coefficient is defined as $c = 2\zeta\rho s\omega$ where ζ is the viscous damping factor. In the present analysis, the adopted viscous damping factor is $\zeta = 0.089$.

3.1. Preliminary results

To check the validity and accuracy of the present methodology, Fig. 2 shows the post-critical path obtained for the empty, axially loaded cylindrical shell, together with those obtained in Refs. [8,4]. All solutions display the same overall behavior: as the axial load increases, the shell loses stability, displaying an initial unstable post-critical path which becomes stable for large-amplitude displacements. Hence, clearly the system loses stability statically via a subcritical bifurcation, displaying a softening nonlinear behavior with a large hysteresis. As can be observed, the shell loses stability at $P/P_{\mathrm{cr}} = 0.954$, a value that is only 0.73 percent higher than in Ref. [8]. The unstable post-critical path shows slightly larger displacements than those in Ref. [8], and the folding point is at $P/P_{\mathrm{cr}} = 0.325$, which is also 1.02 percent higher than in Ref. [8]. For large-amplitude displacements, the post-critical path obtained is very similar to that in Ref. [8]. In fact, a critical analysis of the literature shows that the post-buckling solution may display small quantitative differences due to small differences in the pre-buckling displacement field and in the assumed modal expansion.

Also, in order to demonstrate the accuracy of the present methodology, the natural frequencies of the fluid-filled cylindrical shell are obtained and the results are compared with the numerical values found in the literature. As shown in Table 1, the frequencies obtained using the linearized Donnell theory for this shell geometry are in good agreement with the results obtained by Pellicano and Amabili [8].

3.2. Post-critical analysis

In this section, the influence of the fluid velocity and initial imperfections on the nonlinear post-critical path of the shell under axial load is analyzed.

Fig. 3 displays the post-critical paths of the perfect shell for increasing fluid flow velocity. As the flow velocity increases, the critical load decreases steadily. For a fluid-filled shell without flow ($U = 0.0$), the bifurcation point is at $P/P_{\mathrm{cr}} = 0.955$ and the folding point is observed at $P/P_{\mathrm{cr}} = 0.325$; for a flow velocity of $U = 0.20U_{\mathrm{cr}}$, the bifurcation point is reduced to a

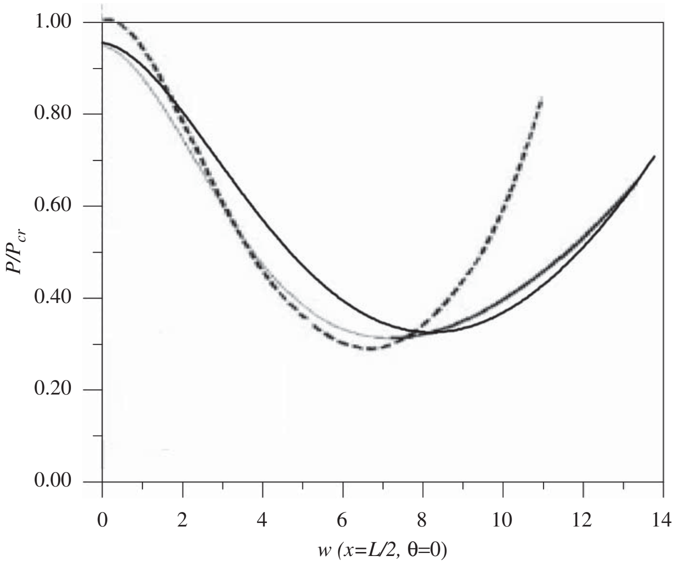

Fig. 2. Comparison of the static post-critical path with previous works. ━━━, Present; ━━━, Ref. [8]; ▬ ▬ ▬, Ref. [4]. For the results from Ref. [8], the gray line represents unstable points and the black line represents stable points.

Table 1
Comparisons of natural frequencies (ω_0) for the fluid-filled shell.

Mode (m,n)	Frequency (Hz)		Present (Hz)	Difference (percent) with Ref. [8]
	Sanders–Koiter Ref. [8]	Donnell Ref. [8]		
(1,5)	260.75	271.26	271.25	0.00
(1,10)	838.75	851.75	851.54	0.02
(3,5)	1165.02	1185.09	1185.09	0.00
(1,0)	1061.91	1091.26	1091.26	0.00
(3,0)	2045.45	2049.77	2049.77	0.00
(5,0)	2529.15	2531.03	2531.02	0.00
(7,0)	2943.56	2944.68	2944.68	0.00
(9,0)	3457.34	3458.12	3458.12	0.00

value of $P/P_{cr} = 0.925$ and the folding point goes down to $P/P_{cr} = 0.241$. For $U = 0.40U_{cr}$ the bifurcation point is further reduced to $P/P_{cr} = 0.831$ and there no longer exists a physically meaningful folding point. For the same load level, the large-amplitude displacements are higher as the flow velocity increases. The results in Fig. 3 show the great influence of the flow velocity on the nonlinear behavior of the shell. Not only the critical load is reduced, but the hysteresis is accentuated.

Fig. 4 shows the combined effect of flowing fluid and imperfections on the response of the axially loaded cylindrical shell. Fig. 4(a) illustrates the nonlinear responses of the imperfect shell, considering a flowing fluid with $U = 0.20U_{cr}$ and varying levels of imperfection in the form of the fundamental buckling mode. The results are compared with the response of the perfect shell with $U = 0.0$. Increasing the imperfection magnitude, the value of the limit point in the nonlinear path is reduced considerably. For example, for $\Xi_{1,1} = 0.2$, the value of the upper limit load (load carrying capacity of the imperfect shell) goes down to $P/P_{cr} = 0.746$, which corresponds to a reduction of about 22 percent in relation to the perfect shell. In contrast, the value of the lower folding point does not change significantly with increasing level of imperfection. In Fig. 4(b) the nonlinear post-critical paths are plotted for $U = 0.20U_{cr}$, and varying imperfection components. When imperfections in the first and main axisymmetric mode are considered ($\Xi_{1,1} = 0.2$, $\Xi_{0,2} = 0.2$), the limit point goes down to $P/P_{cr} = 0.663$. This value is about 7 percent lower than the limit point with imperfection only in the fundamental mode ($\Xi_{1,1} = 0.2$). This shows that an imperfection in the form of the nonlinear displacement field, that is, including the linear vibration mode plus the main axisymmetric component with twice the number of waves in the axial direction, leads to higher imperfection sensitivity. If imperfection is considered in higher modes, the limit point load increases instead of decreasing, showing that the nonlinear dynamics is sensitive to the form of imperfection. Fig. 4(c) provides a curve depicting the imperfection sensitivity of the upper limit load. As can be seen, the flow reduces the value of the limit load as compared to the curve with only static fluid; and, as the magnitude of imperfection increases, the value of the limit load is strongly reduced.

One must keep in mind that, due to the fabrication process, installation and environment, cylindrical shells are subjected to complex imperfection patterns. However, as shown by Batista [32] through the expansion of mapped

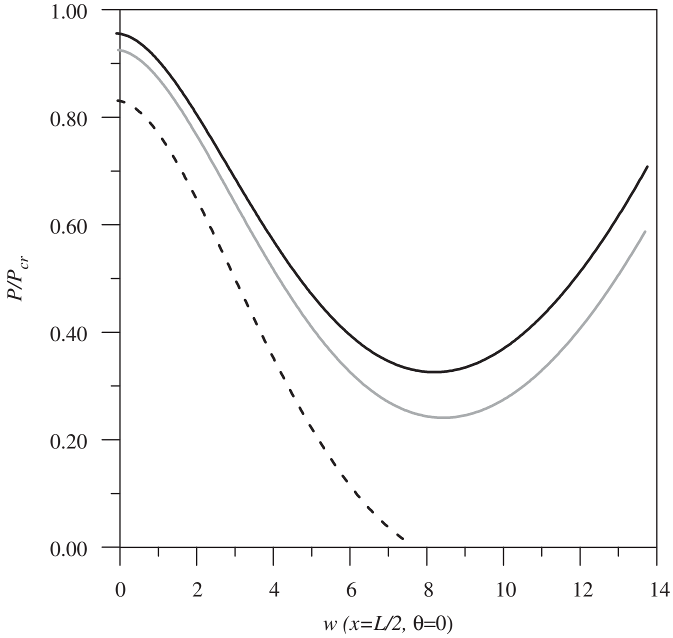

Fig. 3. Post-critical paths of the perfect shell for increasing fluid flow velocity. ▬▬▬, $U = 0.0$; ▬▬▬, $U = 0.20U_{\mathrm{cr}}$; ▬ ▬ ▬, $U = 0.40U_{\mathrm{cr}}$.

imperfections of several thin shell surfaces in Fourier series, the pattern is usually dominated by modes with long wavelengths in the axial direction similar to the buckling mode. This is also observed in the large collection of experimental data stored in the initial imperfection data bank at Delft University of Technology [33]. So, it is expected that the nonlinear response will be dominated by these components, which explains the low buckling values obtained experimentally [1,31]. Also, the unsteady component of the fluid flow can be viewed as a kind of imperfection.

3.3. Dynamic analysis without external force

In Fig. 5 the frequencies, parameterized in relation to the natural frequency of the empty shell ($\omega_{0e} = 3165.93$ rad/s), are plotted as a function of the vibration amplitude of the first mode, and imperfections are considered only in the first mode, $\xi_{1,1}$. Fig. 5(a) displays the frequency–amplitude relation of the perfect shell with no static pre-load, considering both empty and fluid-filled shell with varying flow velocity. As one can observe, comparing with the response of the empty shell, for a quiescent fluid, the natural frequency of the shell is reduced and the degree of the softening nonlinearity increases. When the curve bends back, due to large flexural deformations, large-amplitude displacements are associated with smaller frequency values. If fluid flow is considered, for example $U = 0.20U_{\mathrm{cr}}$, the natural frequency of the shell is reduced by about 3 percent, and the softening character of the nonlinear response increases even more. For $U = 0.40U_{\mathrm{cr}}$, the shell shows a stronger softening behavior with no bending back. In Fig. 5(b) the frequency–amplitude relations are plotted for an imperfect shell and no static pre-loading. The initial geometric imperfections do not have a great influence on the natural frequencies, but they change the degree of nonlinearity of the response. The initial branch of the curves displays a more pronounced softening behavior as the level of imperfection is increased; however, after the folding point, the amplitudes are smaller with increasing imperfection.

Figs. 5(c) and (d) show the effect of the static pre-loading ($P_e = 0.50P_{\mathrm{cr}}$) on the natural frequency of the perfect and imperfect shell. In Fig. 5(c) the natural frequencies are reduced due to the influence of the static load and also the softening of the curve is highly enhanced. Finally, Fig. 5(d) shows the effect of initial imperfections in the first mode for the pre-loaded shell. In this case, the imperfect curve converges to the path of the perfect shell but the natural frequencies are reduced by the imperfection.

Fig. 6 shows the variation of the natural frequencies of the shell with the flow velocity and imperfection level ($P_e = 0.0$). The natural frequencies are parametrized in relation to the natural frequency of the fluid-filled shell, ω_0. Imperfections are considered to have the form of the corresponding linear vibration mode with $\Xi_{1,1} = 0.4$, 0.6 and 0.8, respectively. In this case the influence of the initial geometric imperfections is smaller than the influence of the flow velocity. For example, for an imperfection in the first mode, $\Xi_{1,1} = 0.4$, the frequency ratio is $\omega/\omega_0 = 0.99$, while for $\Xi_{1,1} = 0.8$, the frequency ratio is $\omega/\omega_0 = 0.97$. As the flow velocity increases, the natural frequencies decrease, becoming zero at the critical velocity value; this is a function of the imperfection magnitude. For an imperfection equal to $\Xi_{1,1} = 0.4$ the critical velocity ratio is $U/U_{\mathrm{cr}} = 0.98$, and for $\Xi_{1,1} = 0.8$ the critical velocity ratio goes down to $U/U_{\mathrm{cr}} = 0.96$.

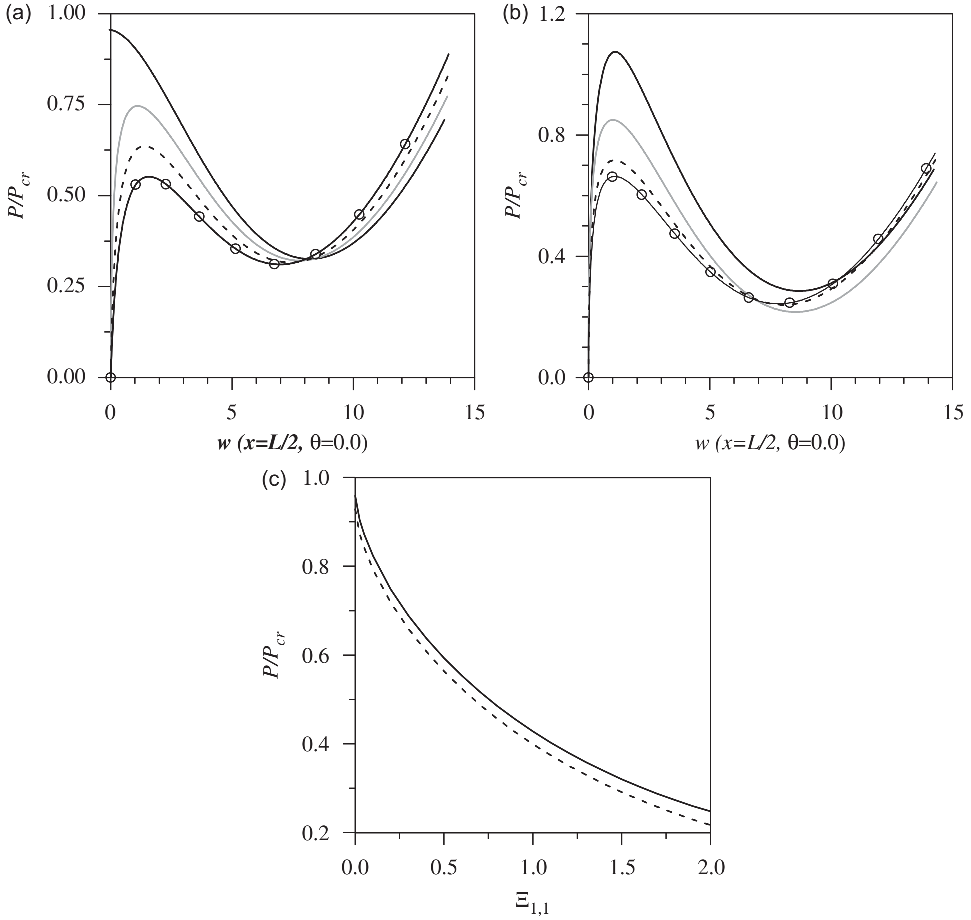

Fig. 4. Influence of flow velocity and imperfections on the post-critical response of the shell: (a) ——, $U = 0.0$, perfect shell; ——, $U = 0.20U_{cr}$, $\Xi_{1,1} = 0.2$; ■■■■■■, $U = 0.20U_{cr}$, $\Xi_{1,1} = 0.4$; —⊖—, $U = 0.20U_{cr}$, $\Xi_{1,1} = 0.6$; (b) $U = 0.20U_{cr}$, and ——, $\Xi_{1,1} = 0.2$, $\Xi_{0,1} = 0.2$, $\Xi_{0,3} = 0.2$, $\Xi_{0,4} = 0.2$; ——, $\Xi_{1,1} = 0.2$, $\Xi_{0,2} = 0.2$, $\Xi_{0,3} = 0.2$; ■■■■■■, $\Xi_{1,1} = 0.2$; —⊖—, $\Xi_{0,2} = 0.2$; (c) imperfection sensitivity curve. ——, $U = 0.0$; ■■■■■■, $U = 0.20U_{cr}$.

3.4. Dynamic analysis including harmonic axial load

Now the simultaneous effect of the harmonic axial load, i.e., $P_d \neq 0$, and of the flow velocity on the nonlinear vibrations of the shell is considered.

First, the parametric instability of the perfect shell is studied considering for each value of the excitation frequency, ω, an increasing axial loading, P_d, cf. Eq. (1). Fig. 7 shows the numerically obtained bifurcation boundaries for a slowly evolving system in the frequency/excitation–amplitude control space for the perfect shell. The shell is axially pre-loaded with $P_e = 0.30P_{cr}$, the fluid flow velocity is equal to either $U = 0$ or $U = 0.20U_{cr}$. The frequency of excitation is parametrized by the natural frequency of the fluid-filled shell ($\omega_0 = 1704.33$). The natural frequency of the pre-loaded shell ($P_e = 0.30\,P_{cr}$) is equal to $\omega_{0L} = 1384.63$ rad/s ($\omega_{0L}/\omega_0 = 0.81$). The parametric instability boundary is the limit where small perturbations from the trivial solution will result in an initial exponential growth in the oscillations. This boundary is obtained by increasing slowly the excitation amplitude of P_d while holding the frequency constant. The parametric instability boundary is composed of various curves, each one associated with a particular bifurcation event. The first important instability region is associated with the direct resonance zone, $\omega/\omega_0 = 0.81$, when the frequency of excitation is equal to the lowest natural frequency of the pre-loaded shell ($\omega = \omega_{0L}$). The second well to the right is associated to the principal parametric instability region and occurs around $\omega/\omega_0 = 1.62$, when the frequency of excitation is equal to two times the natural frequency of the pre-loaded shell ($\omega = 2\omega_{0L}$). The upper region of the instability boundary, between the first and second regions, shows a kind of fractal boundary. When comparing the boundaries of the system with and without flow, it is possible to observe that the fluid velocity has the effect of shifting all the instability boundaries to the left. So, the flow velocity may increase or decrease the critical load, depending on the value of the forcing frequency. For axial static pre-loads lower than the minimum post-critical load, which corresponds to a saddle-node bifurcation (see Figs. 2–4), the shell potential energy has only one potential well and after the parametric instability various types of motion may be

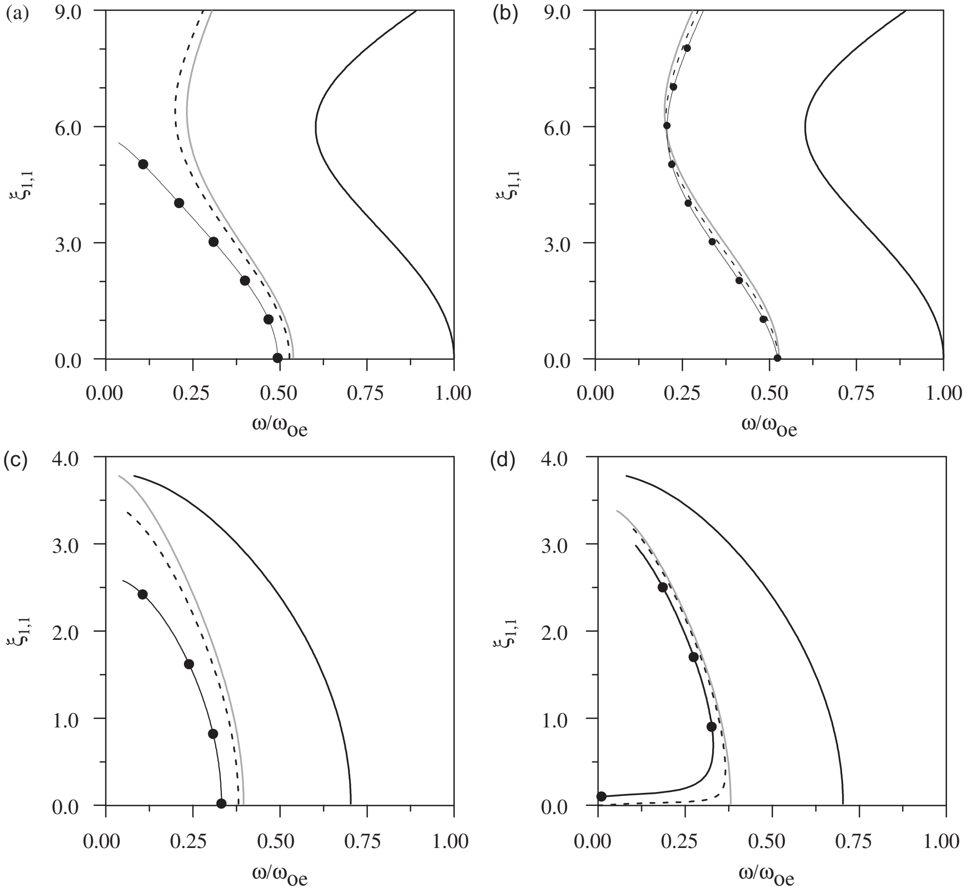

Fig. 5. Influence of static load, flow velocity and imperfections on the frequency–amplitude relation. (a) Perfect shell, $P_e = 0.0$ and: ——, empty; ——, $U = 0.0$; ■■■■■■, $U = 0.20U_{cr}$; —●—, $U = 0.40U_{cr}$; (b) $P_e = 0.0$ and: ——, perfect empty; ——, perfect, $U = 0.0$; ■■■■■■, $U = 0.40U_{cr}$, $\Xi_{1,1} = 0.20$; —●—, $U = 0.40U_{cr}$, $\Xi_{1,1} = 0.40$; (c) perfect shell, $P_e = 0.50P_{cr}$ and: ——, empty; ——, $U = 0.0$; ■■■■■■, $U = 0.20U_{cr}$; —●—, $U = 0.40U_{cr}$; (d) $P_e = 0.50P_{cr}$ and: ——, perfect empty; ——, perfect, $U = 0.0$; ■■■■■■, $U = 0.20U_{cr}$, $\Xi_{1,1} = 0.2$; —●—, $U = 0.20U_{cr}$, $\Xi_{1,1} = 0.10$. Here $\omega_{0e} = 3165.029$ rad/s is the natural frequency of the empty shell.

observed within this well. For static load levels higher than the minimum post-critical load, the shell potential energy displays three potential wells [34] and, after the parametric instability occurs, the system may remain within the pre-buckling well, escape to a post-buckling well or exhibit large cross-well motions.

Fig. 8 shows typical bifurcation diagrams associated with the two main instability regions due to the variation of the axial load, for different values of the excitation frequency and $U = 0.20U_{cr}$. The shell is axially pre-loaded with $P_e = 0.30P_{cr}$. This value is higher than the minimum post-critical load for the adopted conditions. These bifurcation diagrams are obtained by the brute-force method, together with continuation techniques by increasing the forcing amplitude. The bifurcation diagrams depicted in Figs. 8(a)–(c) are typical of the resonance region around $\omega/\omega_0 = 0.81$. In Fig. 8(a), after the critical point, $P_b = 0.61$, the trivial solution becomes unstable and the system displays large-amplitude cross-well chaotic oscillations. In this case, close to the bifurcation point, any small perturbation leads to escape from the pre-buckling well (dynamic buckling) and the onset of complex aperiodic motions. In contrast, in Figs. 8(b) and (c), for the slowly evolving system, the trivial solution loses its stability and gives rise to a small-amplitude 1T stable periodic motion within the pre-buckling well. This solution grows in amplitude until the escape load, which corresponds to the complete annihilation of the basin of attraction of this 1T solution, is reached [34]. Beyond this point, only large cross-well motions, such as those depicted in Fig. 8(a), are observed. In the notation used in the paper, a kT periodic motion means a harmonic ($k = 1$) or subharmonic oscillation ($k > 1$) with a period of k times that of the forcing period T. Another branch of 1T solutions also emerge from the critical point, P_b, which is symmetric to the ones shown in Figs. 8(b) and (c).

The bifurcation diagrams depicted in Figs. 8(d)–(f) are typical of the principal region of parametric instability (around $\omega/\omega_0 = 1.62$). Fig. 8(d) shows a typical bifurcation diagram of the descending branch of this region ($\omega < 2\omega_0$), $\omega/\omega_0 = 1.50$. In this case, the parametric bifurcation point corresponds to a subcritical bifurcation of the trivial solution, giving rise to a 2T unstable periodic motion. This unstable solution becomes stable at a saddle-node bifurcation. So, when the load reaches the critical value, depending on the initial conditions, the response may jump to the stable period-two solution within the pre-buckling well or escape from this well. In this case escape is indeterminate. In fact, between the load associated with

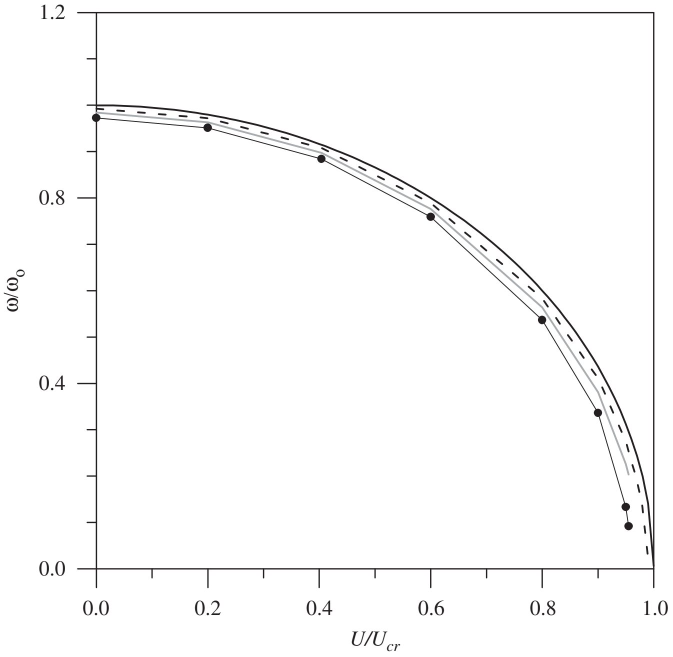

Fig. 6. Variation of natural frequency with fluid flow velocity and imperfections for $P_e = 0.0$, ——, perfect; ■■■■■■, $\Xi_{1,1} = 0.40$; ——, $\Xi_{1,1} = 0.60$; —●—, $\Xi_{1,1} = 0.80$.

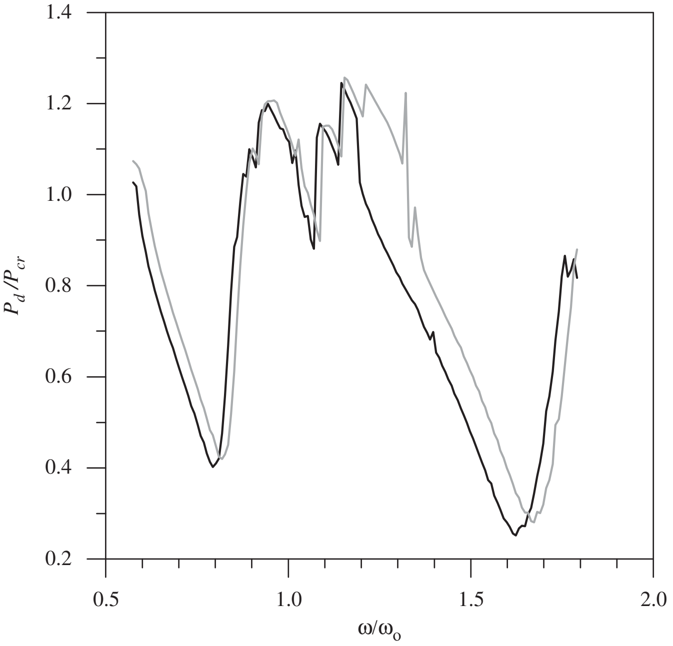

Fig. 7. Instability boundaries in the excitation force control space for a perfect shell with $P_e = 0.30P_{\mathrm{cr}}$ and $\omega_0 = 1704.33$ rad/s. (a) ——, $U = 0.20U_{\mathrm{cr}}$; (b) ——, $U = 0.0$.

the saddle-node bifurcation and that of the subcritical bifurcation, two stable solutions coexist within the pre-buckling well. Fig. 8(e) corresponds to the deepest point of this well and a limit case between subcritical and supercritical bifurcation. After this point, along the ascending stability boundary in Fig. 7, as illustrated in Fig. 8(f) for $\omega/\omega_0 = 1.70$, the parametric bifurcation point corresponds always to a supercritical bifurcation of the trivial solution and describes a $2T$ stable periodic motion. This sequence of bifurcations is typical of softening systems under parametric excitation [35].

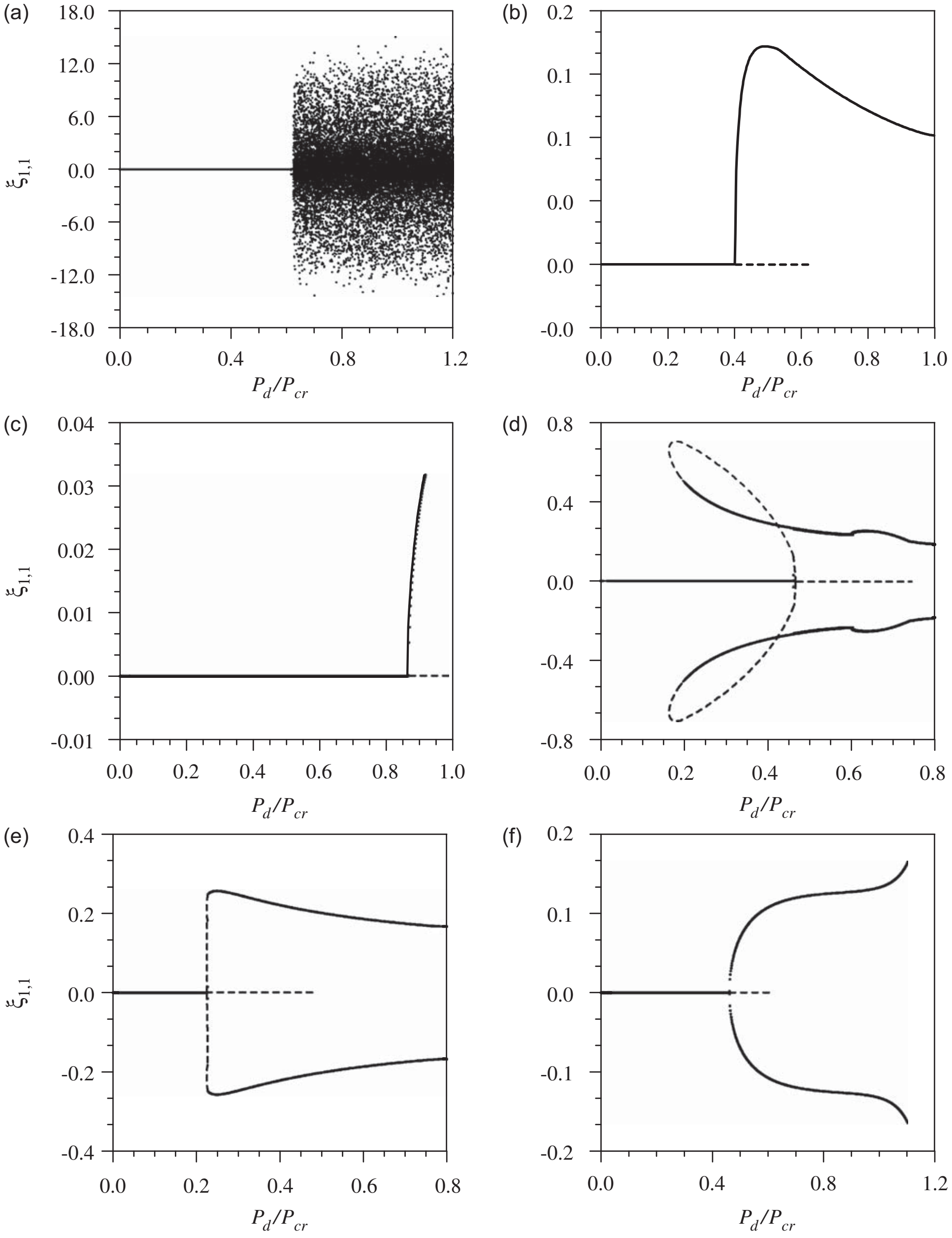

Fig. 8. Escape mechanisms for the instability diagram for the perfect shell with $P_e = 0.30P_{\text{cr}}$ and $U = 0.20U_{\text{cr}}$. (a) $\omega/\omega_0 = 0.70$, $P_b = 0.61$; (b) $\omega/\omega_0 = 0.81$, $P_b = 0.40$; (c) $\omega/\omega_0 = 0.85$, $P_b = 0.87$; (d) $\omega/\omega_0 = 1.50$, $P_b = 0.46$; (e) $\omega/\omega_0 = 1.62$, $P_b = 0.22$; (f) $\omega/\omega_0 = 1.70$, $P_b = 0.46$. P_b represents bifurcation load, ▬▬, stable points and ‒ ‒ ‒, unstable points.

Fig. 9 depicts the bifurcation diagrams of the imperfect shell with $\Xi_{1,1} = 0.2$. For comparison, these diagrams are plotted for the same values of excitation frequency as those in Fig. 8. The shell is again pre-loaded axially with $P_e = 0.30P_{\text{cr}}$ and the internal fluid flow velocity is $U = 0.20U_{\text{cr}}$. When comparing the bifurcation diagrams in Fig. 8 with the corresponding ones in Fig. 9, the expected influence of the initial geometric imperfections on the nonlinear behavior of the shell and critical loads becomes clear. One must keep in mind that in this case the trivial solution no longer exists due to the flexural deformations induced by the imperfection. A zoomed version of the non-trivial solution is shown in Fig. 10, where the initial branches of the bifurcation diagrams are obtained by continuation techniques [26].

Figs. 9(a)–(c) and 10(a)–(c) show the bifurcation diagrams related to the instability region around $\omega/\omega_0 = 0.81$. In Fig. 9(a), as the axial load increases, a branch of non-trivial 1*T* stable periodic motion within the pre-buckling well appears with the first bifurcation occurring at $P_d/P_{\text{cr}} = 0.25$, where a small jump occurs. As shown in Fig. 10(a) there is here a small loop with two saddle-node bifurcations separating two branches of 1*T* stable solutions. However, the solutions remain

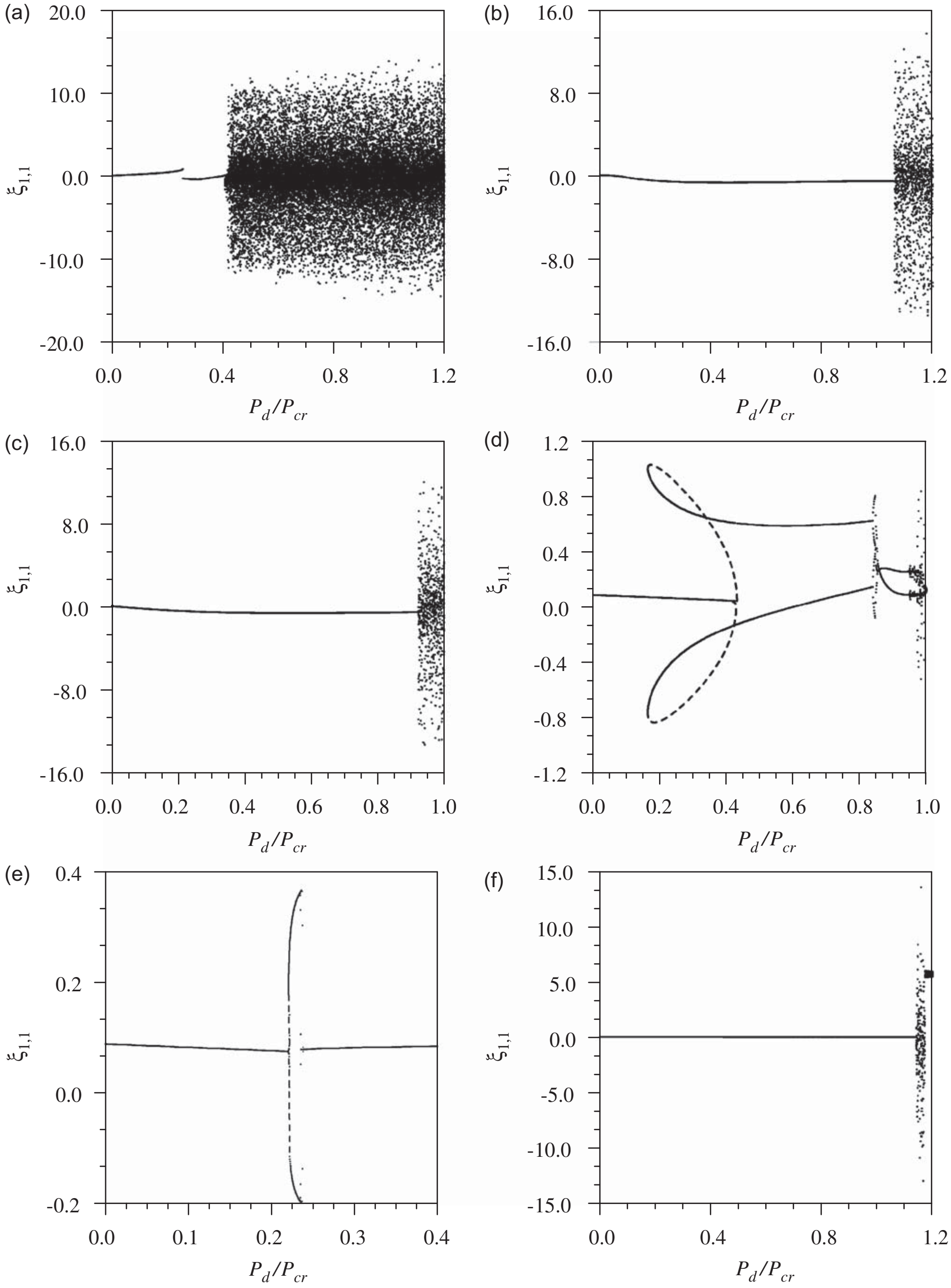

Fig. 9. Parametric instability and escape mechanisms for the imperfect shell with $\Xi_{1,1} = 0.2$; $P_e = 0.30P_{\text{cr}}$ and $U = 0.20U_{\text{cr}}$. (a) $\omega/\omega_0 = 0.70$, $P_b = 0.25$; (b) $\omega/\omega_0 = 0.81$, $P_b = 1.06$; (c) $\omega/\omega_0 = 0.85$, $P_b = 0.92$; (d) $\omega/\omega_0 = 1.50$, $P_b = 0.43$; (e) $\omega/\omega_0 = 1.62$, $P_b = 0.22$; (f) $\omega/\omega_0 = 1.70$, $P_b = 0.46$.

within the pre-buckling well. Finally, as the axial load increases, the ensuing small-amplitude 1*T* solution becomes unstable and the shell escapes from the pre-buckling well, displaying large-amplitude chaotic motions. Figs. 9(b) and 10(b) correspond to the deepest point of this instability region and no bifurcation is observed previous to escape. The response corresponds to a small-amplitude 1*T* oscillation induced by the imperfection. Again, after escape, the shell exhibits large cross-well chaotic oscillations. In Fig. 9(c) the shell displays almost the same behavior as that described in Fig. 9(b).

Figs. 9(d)–(f) show the bifurcation diagrams related to the principal parametric instability region at $\omega/\omega_0 = 1.62$. In Fig. 9(d) the shell displays a subcritical bifurcation similar to that in Fig. 8(d), but the bifurcated steady-state solution is no longer symmetric with respect to the $\xi_{1,1}$ coordinate, as in Fig. 8(d). This can be clearly observed in Fig. 10(d). This loss of symmetry is another effect of the geometric imperfections on the dynamic behavior of the shell. In Fig. 9(e), the bifurcation is now supercritical with practically the same value of the parametric instability load as in the perfect case. However, the 2*T*

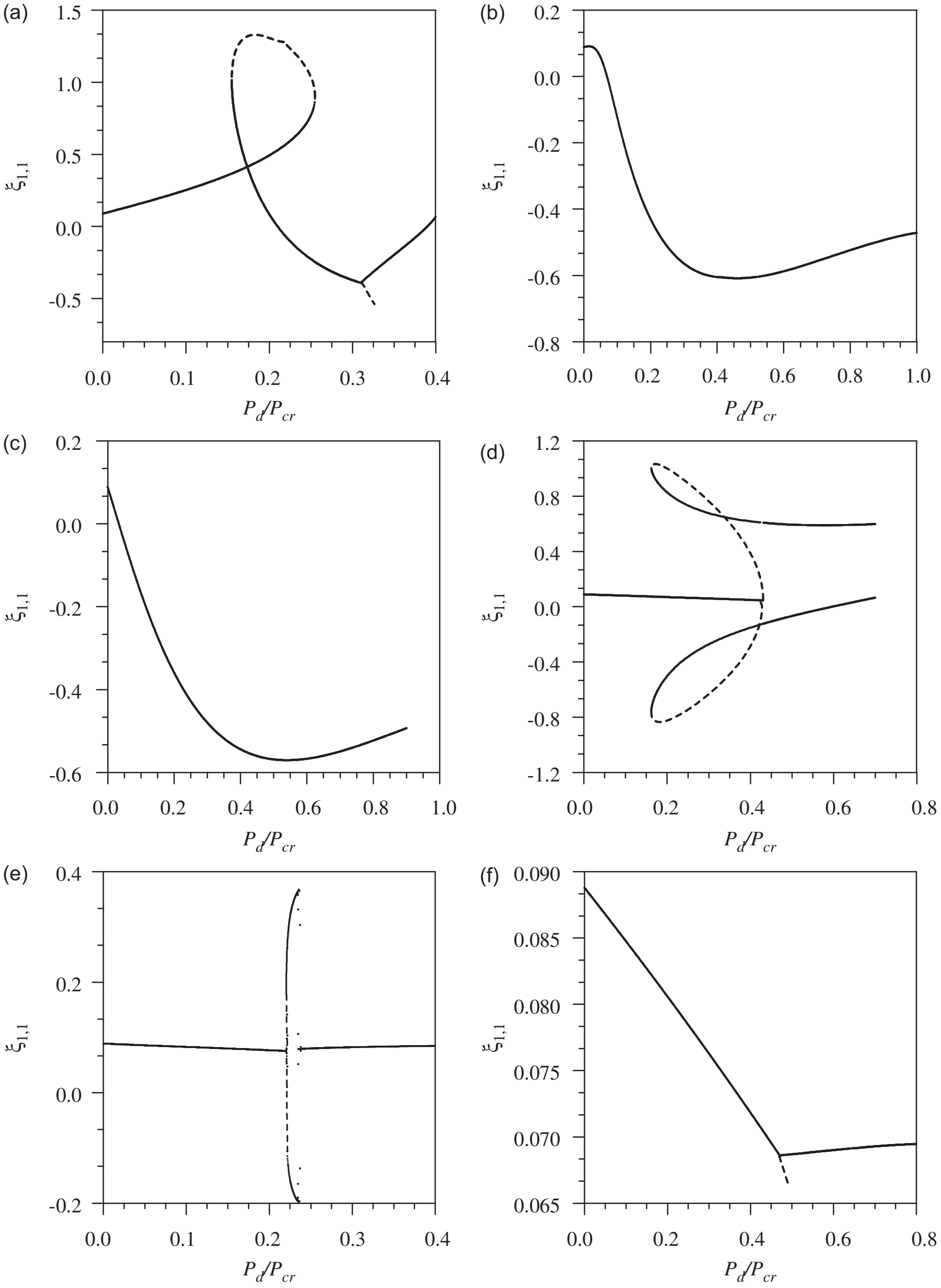

Fig. 10. Parametric instability and escape mechanisms for the imperfect shell with $\Xi_{1,1} = 0.2$; $P_e = 0.30P_{\mathrm{cr}}$ and $U = 0.20U_{\mathrm{cr}}$. (a) $\omega/\omega_0 = 0.70$, $P_b = 0.25$; (b) $\omega/\omega_0 = 0.81$, $P_b = 1.06$; (c) $\omega/\omega_0 = 0.85$, $P_b = 0.92$; (d) $\omega/\omega_0 = 1.50$, $P_b = 0.43$; (e) $\omega/\omega_0 = 1.62$, $P_b = 0.22$; (f) $\omega/\omega_0 = 1.70$, $P_b = 0.46$. P_b represents bifurcation load.

solution after a small increase in the forcing magnitude collapses to a 1*T* solution that remains stable up to the escape load. Finally, in Fig. 9(f), as the value of the axial load increases a local bifurcation occurs at $P_d/P_{\mathrm{cr}} = 0.44$, rather different from that observed in Fig. 8(f), giving rise to two branches of 1*T* solutions, one stable and one unstable, as illustrated in Fig. 10(f). From the results presented in Figs. 8–10, one can observe that the imperfection sensitivity of the escape load as well as the load at which the first bifurcation occurs in the pre-buckling well, P_b, depend not only on the imperfection level, as in the static case, but also on the forcing frequency.

Fig. 11 displays the effect of the fluid velocity on the nonlinear oscillations of a perfect shell with no static pre-loading, subjected to a dynamic load of constant magnitude equal to $P_d = 0.7P_{\mathrm{cr}}$. The bifurcation diagrams are plotted considering as control parameter the fluid velocity for three different ratios of the frequency of excitation: $\omega/\omega_0 = 0.90$, 1.34 and 1.80,

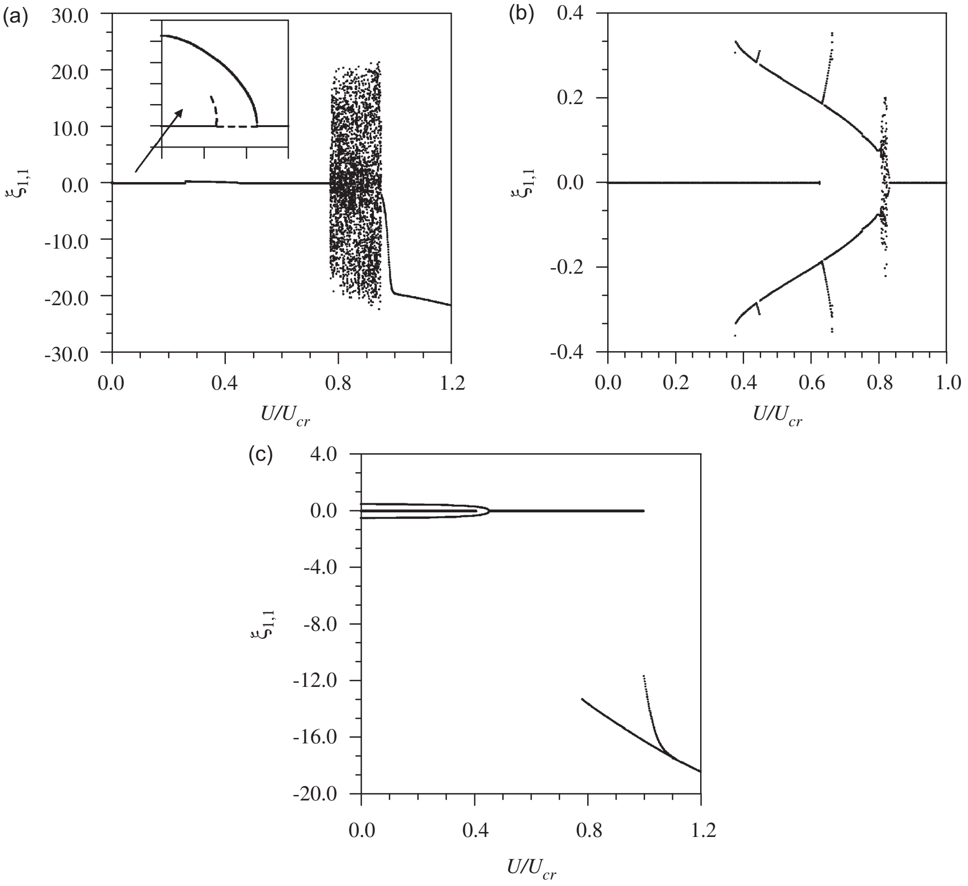

Fig. 11. Effect of flow velocity (U) on the non-linear dynamics of the shell for $P_e = 0.0P_{\mathrm{cr}}$, $P_d = 0.7P_{\mathrm{cr}}$ and $\omega_0 = 1704.36$ rad/s. Perfect shell. (a) $\omega/\omega_0 = 0.90$, $P_b = 0.26$; (b) $\omega/\omega_0 = 1.34$, $P_b = 0.63$; (c) $\omega/\omega_0 = 1.80$, $P_b = 0.41$. P_b represents bifurcation load.

where $\omega_0 = 1704.36$ rad/s is the natural frequency of the fluid-filled shell. The bifurcation diagrams considering varying flow velocity are obtained by increasing and decreasing the flow velocity ratio between 0 and 1.2, so coexisting solutions can be obtained. It is important to notice that not all possible coexisting solution branches are obtained by this process. In fact, to be sure that all co-existing solutions are obtained one should investigate all initial conditions in the region of interest in the 12-dimensional phase-space, which is an almost impossible task. The objective of the present study is only to detect the changes caused by static pre-load, imperfections and flow velocity when one control parameter varies slowly.

Fig. 11(a) depicts the bifurcation diagram for $\omega/\omega_0 = 0.90$. As can be observed in the inset diagram, the shell starts with trivial oscillations and, at a certain point, it exhibits a jump to a 1T small-amplitude oscillation which decreases in magnitude as flow velocity increases and, after a certain value of the fluid flow velocity, the response becomes again trivial. The bifurcations connected with these events are shown in the inset zoomed figure, where the first bifurcation corresponds to a subcritical bifurcation. As the flow velocity increases still further, the shell escapes and oscillations become chaotic and the shell exhibits large cross-well motions. If the frequency of excitation is increased to $\omega/\omega_0 = 1.34$, the shell exhibits a different behavior, as shown in Fig. 11(b). In this case, the first bifurcation point corresponds to a subcritical bifurcation, and the trivial solution loses its stability giving rise to a 2T unstable periodic motion. The jump is indeterminate, because the response may stabilize within the pre-buckling well or jump to a remote attractor. Along the post-critical branch of the bifurcation diagram several bifurcations occurs as the flow velocity increases. They correspond to pitchfork bifurcations, giving rise to two stable 2T coexisting oscillations. However, in each case, the new solution disappears just after a small increase in the control parameter. If flow velocity is further increased, the 2T solution decreases in amplitude, a small chaotic window is observed and, after that, only the in-well trivial solution and large-amplitude solutions coexist. Fig. 10(c) shows the bifurcation diagram for $\omega/\omega_0 = 1.80$. The solution starts with two different attractors, one of period 2T, inside the pre-buckling well, and the trivial solution. As the flow velocity increases, the 2T solution disappears and only the trivial solution remains; at a certain value of the flow velocity, the shell jumps to a 1T large-amplitude solution. The two branches related to large-amplitude cross-well motions are associated with two 1T stable solutions. The results show that a shell under varying flow velocity may display several bifurcation phenomena, giving rise to a rich and complex dynamics. The

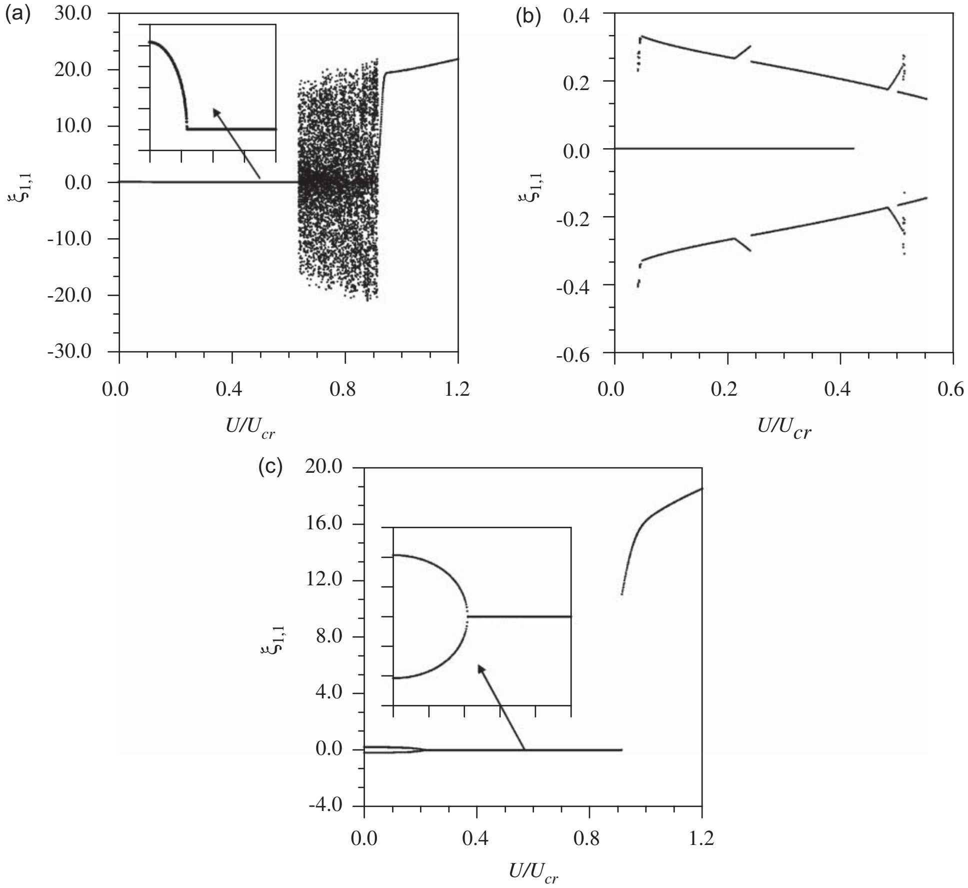

Fig. 12. Effect of flow velocity (U) on the non-linear dynamics of the shell for $P_e = 0.20P_{cr}$, $P_d = 0.7P_{cr}$ and $\omega_0 = 1704.36$ rad/s. Perfect shell. (a) $\omega/\omega_0 = 0.90$, $U_b = 0.12$; (b) $\omega/\omega_0 = 1.34$, $U_b = 0.42$; (c) $\omega/\omega_0 = 1.80$, $U_b = 0.21$. U_b represents bifurcation flow.

existence of several solution branches may lead to undesirable jumps between competing solutions in the presence of small external disturbances.

Fig. 12 shows the simultaneous effect of the static pre-load ($P_e = 0.20P_{cr}$,) and flowing fluid on the nonlinear vibrations of the perfect shell subjected to a harmonic loading of constant magnitude ($P_d = 0.7P_{cr}$). The bifurcation diagrams are plotted for the same frequency ratios selected in Fig. 11: $\omega/\omega_0 = 0.90$, 1.34 and 1.80, where, as before, ω_0 is the natural frequency of the fluid-filled shell. Comparing Figs. 11 and 12, one can observe almost the same general behavior, but critical loads and the length of the stable branches are rather different, illustrating the influence of static pre-load on the shell dynamics.

Fig. 13 displays the effect of geometric imperfections on the nonlinear dynamics of the pre-loaded shell, considering an increasing fluid flow velocity. The bifurcation diagrams are plotted for the same loading conditions as those of Fig. 12, but now an initial geometric imperfection with magnitude equal to $\Xi_{1,1} = 0.2$ is considered.

In Fig. 13, as in previous cases, the trivial solution no longer exists due to the presence of geometric imperfection (see zoomed insets of the initial branches in Fig. 13). For $\omega/\omega_0 = 0.90$, Fig. 13(a), the shell displays initially a 1T small-amplitude oscillation and, at a certain critical value, escape occurs and the solution becomes chaotic. As the fluid flow velocity increases still further, the chaotic vibrations destabilize and a large-amplitude 1T attractor appears. A similar behavior is observed in Fig. 13(b), for $\omega/\omega_0 = 1.34$. However, in this case, three chaotic windows are observed separated by small-amplitude periodic motion. In Fig. 13(c), for $\omega/\omega_0 = 1.80$, the bifurcation diagram exhibits a stable 1T solution till escape to a large-amplitude 1T cross-well motion. Again, the effect of imperfections is quite remarkable, changing completely the shell dynamics.

In the presence of competing solutions, the final behavior of the shell is a function of the initial conditions. The influence of initial conditions can be appraised through the basins of attraction for an appropriate set of initial conditions. To illustrate this, Fig. 14 displays the evolution of the basins of attraction for increasing values of dynamic load, considering $\omega/\omega_0 = 1.50$, $P_e = 0.20P_{cr}$, $U = 0.20U_{cr}$. These results are associated with the bifurcation diagrams of Figs. 8(d) and 9(d) and cover the same set of initial conditions.

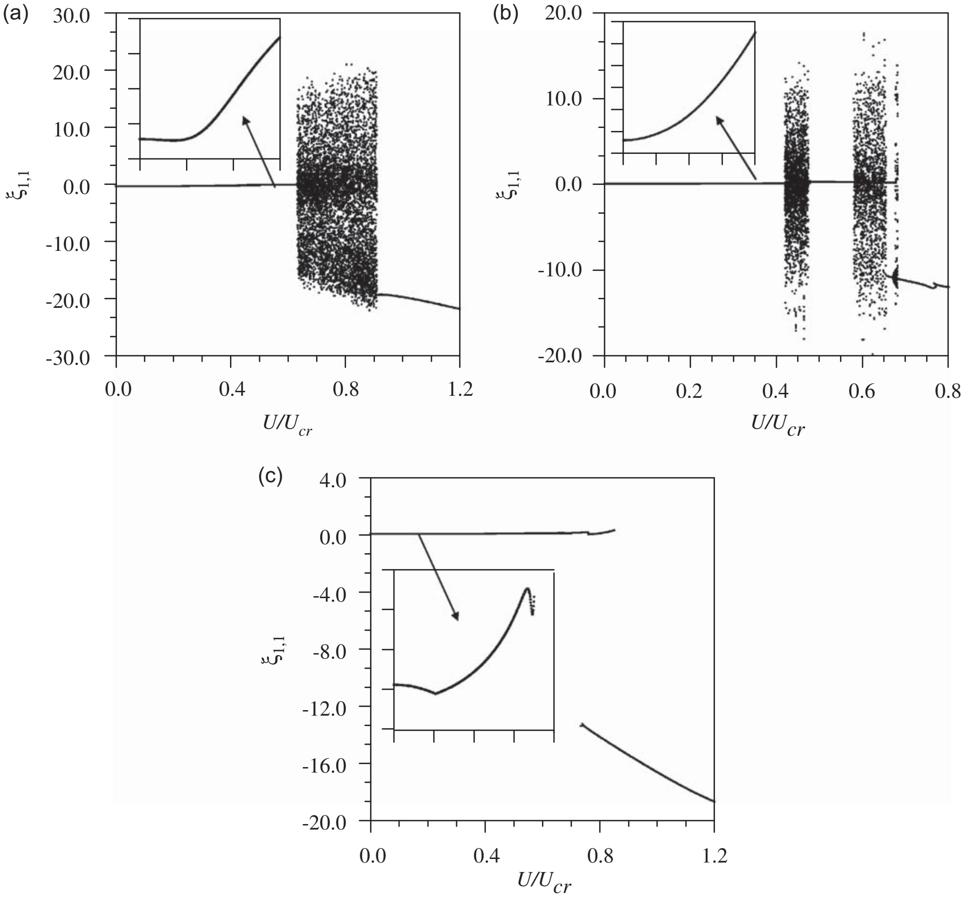

Fig. 13. Effect of flow velocity (U) on the non-linear dynamics of the shell for $P_e = 0.20P_{\mathrm{cr}}$, $P_d = 0.7P_{\mathrm{cr}}$, and $\omega_0 = 1704.36$ rad/s. Imperfect shell with $\Xi_{1,1} = 0.2$. (a) $\omega/\omega_0 = 0.90$, $U_b = 0.63$; (b) $\omega/\omega_0 = 1.34$, $U_b = 0.42$; (c) $\omega/\omega_0 = 1.80$, $U_b = 0.21$. U_b represents bifurcation flow.

Figs. 14(a)–(c) correspond to cross-sections, for the perfect shell, of the 16-dimensional phase space by the $\xi_{1,1} \times \xi_{0,1}$ plane (the other 14 phase space coordinates are taken as zero). In these figures, the black area corresponds to the trivial solution, the dark gray area to small-amplitude non-trivial solutions within the pre-buckling well, and the white area to large-amplitude cross-well solutions. In Fig. 14(a), for $P_d = 0.10P_{\mathrm{cr}}$, only small perturbations of the trivial solution (small values of the initial conditions) around the stable axisymmetric initial configuration will lead with certainty to the trivial solution. For larger perturbations, the basin of attraction becomes fractal and the initial conditions could lead to either the trivial or large-amplitude solutions. In this case the shell displays a high sensitivity to initial conditions. As the axial load increases (see Fig. 14(b) for $P_d = 0.30P_{\mathrm{cr}}$), the trivial solution and a 2T small-amplitude solution coexist within the pre-buckling well. Again, there is a black continuous region surrounding the trivial solution, but smaller than that in Fig. 14(a). This means that the degree of safety of the trivial solution decreases, and unwanted oscillations may occur in response to a larger set of initial conditions. If small-amplitude 2T oscillations are allowed in design, the stable region is constituted by the sum of the black and gray areas. Again, for large perturbations, the transient perturbed solution may be attracted to one of the three different attractors, leading to high sensitivity to initial conditions. For larger values of the axial load (see Fig. 14(c) for $P_d = 0.50P_{\mathrm{cr}}$), the trivial solution disappears and only the small-amplitude 2T solution within the pre-buckling well and the large-amplitude solution remain. All cross-sections display symmetry with respect to the $\xi_{1,1}$ coordinate, this is a characteristic of the perfect shell.

Figs. 14(d)–(f) correspond to cross-sections of the 16-dimensional phase space by the $\xi_{1,1} \times \xi_{0,1}$ plane for the imperfect shell, considering the imperfection amplitude as $\Xi_{1,1} = 0.2$ and the same load levels as in Figs. 14(a)–(c). The black area corresponds to the non-trivial 1T small-amplitude solution of the imperfect shell, the dark gray area, to the small-amplitude 2T solution and the white gray area to large-amplitude cross-well solutions (see Fig. 9(d)). Comparing Figs. 14(a) and (d), one can see that, due to the imperfection, the black area decreases slightly and the basin becomes distorted with respect to the $\xi_{1,1}$ coordinate. Comparing Figs. 14(b) and (e), the distortion of the basin increases and the safe region related to the 1T solution or the two in-well motions decreases, increasing the probability of escape from the pre-buckling well. Increasing the value of the axial load still further (see Fig. 14(f)), the whole basin area becomes fractal and greatly distorted,

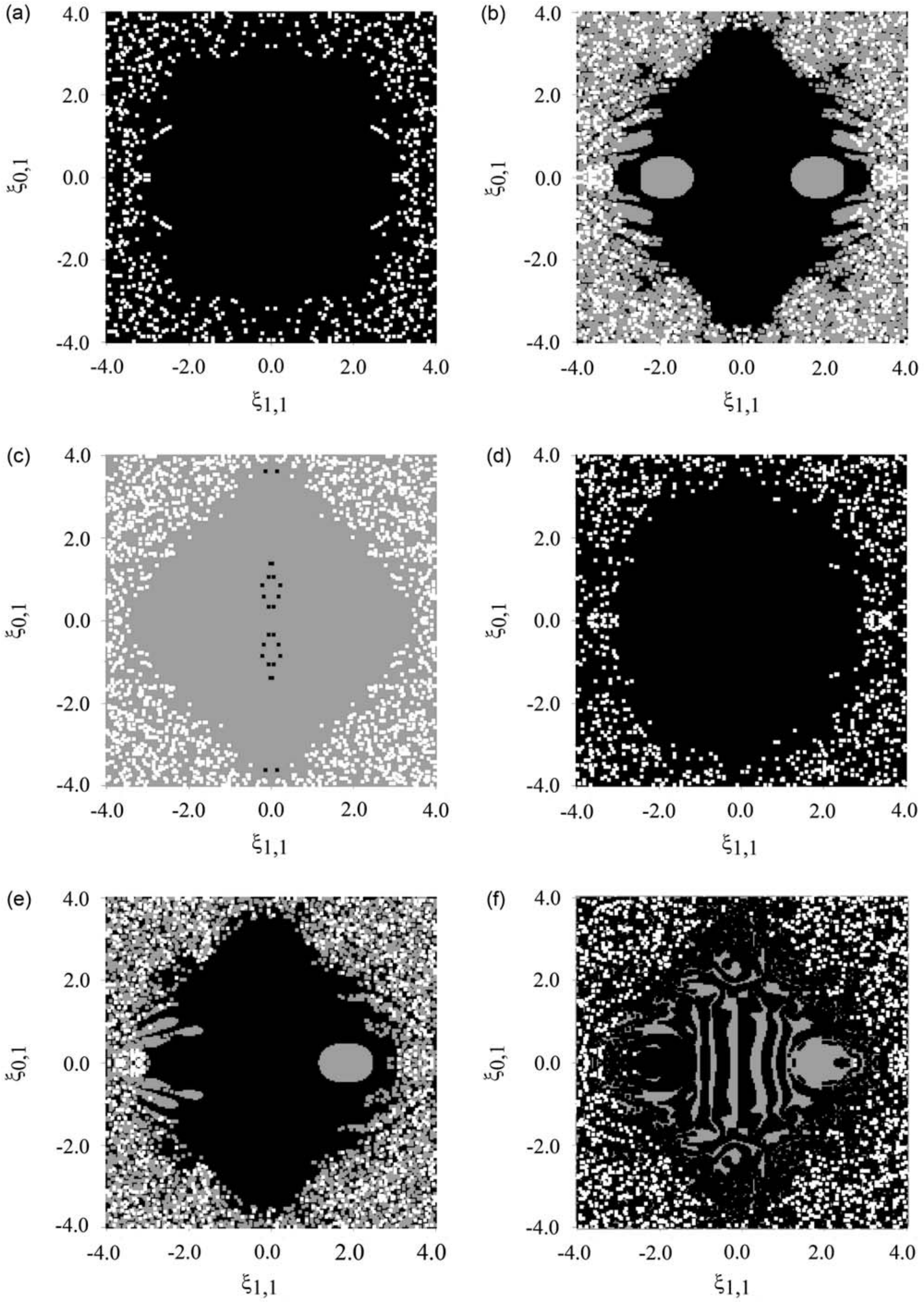

Fig. 14. Basins of attraction for $P_e = 0.30P_{cr}$, $U = 0.20U_{cr}$, $\omega/\omega_0 = 1.50$ and $\omega_0 = 1704.36$ rad/s. Perfect shell: (a) $P_d = 0.10P_{cr}$; (b) $P_d = 0.30P_{cr}$; (c) $P_d = 0.50P_{cr}$. Imperfect shell with $\Xi_1 = 0.2$: (d) $P_d = 0.10P_{cr}$; (e) $P_d = 0.30P_{cr}$; (e) $P_d = 0.50P_{cr}$. Perfect: ■ trivial solution, ▨ non-trivial solution within the pre-buckling well and □ large-amplitude cross-well solution, imperfect: ■ small-amplitude in-well solution, ▨ medium-amplitude in-well solution and □ large-amplitude cross-well solution.

showing a high sensitivity to initial conditions. It is clear from the results that, in order to evaluate the safety of a given solution, not only a detailed analysis of the bifurcations is necessary but also an analysis of the topological characteristics of the basins of attraction. This is particularly important when several solutions coexist for a given set of parameters.

Finally, Fig. 15 displays the evolution of the basins of attraction for increasing values of flowing fluid velocity considering $\omega/\omega_0 = 1.34$, $P_e = 0.20P_{cr}$, $P_d = 0.70P_{cr}$. These results are associated with the bifurcation diagrams of Figs. 12(b) and 13(b) and cover the same set of initial conditions.

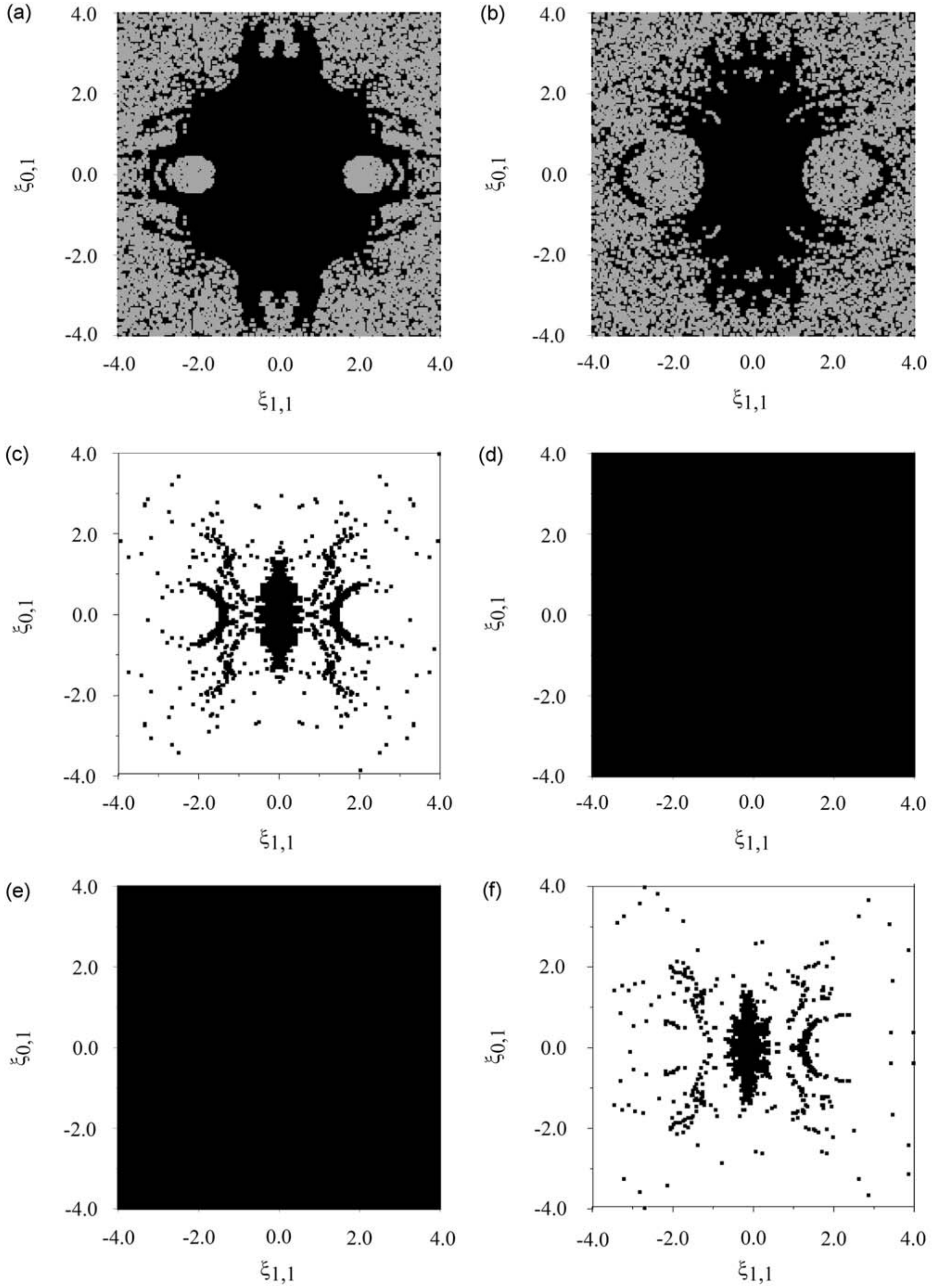

Fig. 15. Basins of attraction for $P_e = 0.20P_{cr}$, $P_d = 0.70P_{cr}$, $\omega/\omega_0 = 1.34$ and $\omega_0 = 1704.36$ rad/s. Perfect shell: (a) $U/U_{cr} = 0.20$; (b) $U/U_{cr} = 0.40$; (c) $U/U_{cr} = 0.80$. Imperfect shell with $\Xi_1 = 0.2$: (d) $U/U_{cr} = 0.20$; (e) $U/U_{cr} = 0.40$ (f) $U/U_{cr} = 0.80$. Perfect: ■ trivial solution, ▨ non-trivial solution within the pre-buckling well and □ large-amplitude cross-well solution, imperfect : ■ small-amplitude in-well solution, ▨ medium-amplitude in-well solution and □ large-amplitude cross-well solution.

Figs. 15(a)–(c) correspond to cross-sections for the perfect shell, while Figs. 15(d)–(f) correspond to cross-sections for the imperfect shell, considering again $\Xi_{1,1} = 0.2$. The color scheme is similar to the one used in Fig. 14. The results illustrate the simultaneous influence of varying fluid velocity and imperfections on the global behavior of the shell.

4. Conclusions

In the present paper the combined effect of initial geometric imperfections and of internal flowing fluid on the nonlinear oscillations and instabilities of cylindrical shells under static and dynamic axial loads has been considered. The influence of the static compressive force on the nonlinear oscillations and escape mechanisms from the pre-buckling potential well has also been investigated.

As demonstrated in the past, the results show that imperfections have a large influence on the static buckling load of the shell. This deleterious effect on the load capacity of the shells increases with the fluid flow velocity. On the other hand, the influence of geometric imperfections on the natural frequencies and on the nonlinear amplitude–frequency relation is smaller.

For the shell under the combined effect of dynamic axial load and fluid flow, parametric instabilities (resonances) occur. The results show that the parametric instability regions are affected by the imperfections and the magnitude of the flow velocity. In this case, the critical load is affected by the forcing frequency, and the imperfection may increase or decrease the parametric instability load. The flow velocity also has a marked influence on the instability boundaries, shifting the stability boundaries to a lower frequency range and decreasing the critical load. The combined effect of geometric imperfections and fluid flow can be understood through a detailed parametric analysis of the bifurcation diagrams. This allows the identification of the type of bifurcation involved and the multiplicity of solutions.

The static pre-load also has a great influence on the results by modifying the potential function of the shell. For static load levels higher than the minimum post-critical load of the shell with fluid flow and lower than the respective critical load, two new wells appear, and escape from the pre-buckling well may occur. Again the critical escape load depends on the static and dynamic load, fluid velocity and initial imperfections. Due to the presence of coexisting attractors, the global behavior of the system can be understood only by an analysis of the basins of the different attractors. The results show that the degree of safety and the whole basin topology change radically under the presence of even small imperfections. Disregarding the effect of imperfections may lead to an erroneous assessment of the degree of safety and robustness of a given configuration, which may have disastrous consequences in engineering practice.

Acknowledgments

This work was made possible by the support of the Brazilian Ministry of Education—CAPES. The support by NSERC of Canada and FQRNT of Québec is also gratefully acknowledged. The second author acknowledges the support by CNPq and FAPERJ-CNE.

References

[1] N. Yamaki, *Elastic Stability of Circular Cylindrical Shells*, North-Holland, Amsterdam, 1984.
[2] R.C. Batista, P.B. Gonçalves, Non-linear lower bounds for shell buckling design, *Journal of Constructional Steel Research* 29 (2) (1994) 101–120.
[3] M.P. Païdoussis, *Fluid Structure Interactions. Slender Structures and Axial Flow*, Vol. 2, Elsevier Academic Press, London, 2004.
[4] P.B. Gonçalves, Z.J.G.N. Del Prado, Non-linear oscillations and stability of parametrically excited cylindrical shells, *Meccanica* 37 (2002) 569–597.
[5] A. El Chebair, M.P. Païdoussis, A.K. Misra, Experimental study of annular-flow-induced instabilities of cylindrical shells, *Journal of Fluids and Structures* 3 (1989) 349–364.
[6] K.N. Karagiozis, M.P. Païdoussis, A.K. Misra, E. Grinevich, An experimental study of the non-linear dynamics of cylindrical shells with clamped ends subjected to axial flow, *Journal of Fluids and Structures* 20 (2005) 801–816.
[7] M. Amabili, F. Pellicano, M.P. Païdoussis, Non-linear dynamics and stability of circular cylindrical shells containing flowing fluid. Part III: truncation effect without flow and experiments,, *Journal of Sound and Vibration* 237 (2000) 617–640.
[8] F. Pellicano, M. Amabili, Dynamic instability and chaos of empty and fluid-filled circular cylindrical shells under periodic axial loads, *Journal of Sound and Vibration* 293 (2006) 227–252.
[9] G. Catellani, F. Pellicano, D. Dall'Asta, M. Amabili, Parametric instability of a circular cylindrical shell with geometric imperfections, *Computers and Structures* 82 (2004) 2635–2645.
[10] M. Amabili, M.P. Païdoussis, Review of studies on geometrically non-linear vibrations and dynamics of circular cylindrical shells and panels, with and without fluid–structure interaction, *Applied Mechanics Reviews* 56 (2003) 349–381.
[11] K.N. Karagiosis, Experiments and Theory on the Non-linear Dynamics and Stability of Clamped Shells Subjected to Axial Fluid Flow or Harmonic Excitation, PhD Thesis, McGill University, Canada, 2005.
[12] M. Amabili, *Non-linear Vibrations and Stability of Shells and Plates*, Cambridge University Press, Cambridge, UK, 2008.
[13] D.A. Evensen, Non-linear flexural vibrations of thin-walled circular cylinders, NASA TN D-4090, 1967.
[14] E.H. Dowell, C.S. Ventres, Modal equations for the non-linear flexural vibrations of a cylindrical shell, *International Journal of Solids and Structures* 4 (1968) 975–991.
[15] J.H. Ginsberg, Large-amplitude forced vibrations of simply supported thin cylindrical shells, *Journal of Applied Mechanics* 40 (1973) 471–477.
[16] J.C. Chen, C.D. Babcock, Non-linear vibration of cylindrical shells, *American Institute of Aeronautics and Astronautics Journal* 13 (1975) 868–876.
[17] P.B. Gonçalves, R.C. Batista, Non-linear vibration analysis of fluid-filled cylindrical shells, *Journal of Sound and Vibration* 127 (1988) 133–143.
[18] M. Amabili, F. Pellicano, M.P. Païdoussis, Non-linear dynamics and stability of circular cylindrical shells containing flowing fluid. Part I: stability, *Journal of Sound and Vibration* 225 (1999) 655–699.
[19] M. Amabili, F. Pellicano, M.P. Païdoussis, Non-linear dynamics and stability of circular cylindrical shells containing flowing fluid. Part II: large-amplitude vibrations without flow, *Journal of Sound and Vibration* 228 (1999) 1103–1124.
[20] M. Amabili, F. Pellicano, M.P. Païdoussis, Non-linear dynamics and stability of circular cylindrical shells containing flowing fluid. Part III: truncation effect without flow and experiments, *Journal of Sound and Vibration* 237 (2000) 617–640.
[21] M. Amabili, F. Pellicano, M.P. Païdoussis, Non-linear dynamics and stability of circular cylindrical shells containing flowing fluid. Part IV: large-amplitude vibrations with flow, *Journal of Sound and Vibration* 237 (2000) 641–666.
[22] L. Watawala, W.A. Nash, Influence of initial geometric imperfections on vibrations of thin circular cylindrical shells, *Computers and Structures* 16 (1983) 125–130.
[23] M. Amabili, F. Pellicano, Multi-mode approach to non-linear supersonic flutter of imperfect circular cylindrical shells, *Journal of Applied Mechanics* 69 (2002) 117–129.
[24] M. Amabili, Theory and experiments for large-amplitude vibrations of empty and fluid-filled circular cylindrical shells with imperfections, *Journal of Sound and Vibration* 262 (2003) 921–975.

[25] F. Pellicano, M. Amabili, Dynamic instability and chaos of empty and fluid-filled circular cylindrical shells under periodic axial loads, *Journal of Sound and Vibration* 293 (2006) 227–252.

[26] E.J. Doedel, A.R. Champneys, T.F. Fairgrieve, Y.A. Kuznetsov, B. Sandstede, X. Wang, *AUTO 97: Continuation and Bifurcation Software for Ordinary Differential Equations (with HomCont)*, Concordia University, Montréal, Canada, 1998.

[27] P.B. Gonçalves, Z.J.G.N. Del Prado, Low-dimensional Galerkin models for non-linear vibration and instability analysis of cylindrical shells, *Non-linear Dynamics* 41 (1–3) (2005) 129–145 (Special issue on Reduced order models: methods and applications).

[28] M. Amabili, A. Sarkar, M.P. Païdoussis, Chaotic vibrations of circular cylindrical shells: Galerkin versus reduced-order models via the proper orthogonal decomposition method, *Journal of Sound and Vibration* 290 (2006) 736–762.

[29] C. Touzé, M. Amabili, Non-linear normal modes for damped geometrically non-linear systems: application to reduced-order modelling of harmonically forced structures, *Journal of Sound and Vibration* 298 (2006) 958–981.

[30] P.B. Gonçalves, F.M.A. Silva, Z.J.G.N. del Prado, Low dimensional models for the nonlinear vibration analysis of cylindrical shells based on a perturbation procedure and proper orthogonal decomposition, *Journal of Sound and Vibration* 315 (2008) 641–663.

[31] D.O. Brush, B.O. Almroth, *Buckling of Bars, Plates and Shells*, McGraw Hill Book Company, New York, 1975.

[32] R. Batista, Lower Bound Estimates for Cylindrical Shell Buckling, PhD Thesis, University College London, 1979.

[33] J. Arbocz, The imperfection data bank, a mean to obtain realistic buckling loads, in: E. Ramm (Ed.), *Buckling of Shells*, Springer, Berlin, 1982, pp. 535–567.

[34] P.B. Gonçalves, F.M.A. Silva, Z.J.G.N. Del Prado, Global stability analysis of parametrically excited cylindrical shells through the evolution of basin boundaries, *Non-linear Dynamics* 50 (2007) 121–145.

[35] M.S. Soliman, P.B. Gonçalves, Chaotic behavior resulting in transient and steady state instabilities of pressure-loaded shallow spherical shells, *Journal of Sound and Vibration* 259 (2003) 497–512.